Enhanced temperature control performance in underground refuge chambers through optimization of air inlets layout

Haishan Yang[a], Zujing Zhang[a,*], Jiri Zhou[b], Ruiyong Mao[a], Hongwei Wu[c], Xing Liang[d]

[a] College of Civil Engineering, Guizhou Provincial Key Laboratory of Rock and Soil Mechanics and Engineering Safety, Guizhou University, Guiyang, 550025, China.

[b] China MCC5 Group CORP.LTD., MCC5 Tower, No.9 Wuye Road, Jinjiang District, Chengdu, 610000, China.

[c] School of Physic, Engineering and Computer Science, University of Hertfordshire, Hatfield, AL10 9AB, UK.

[d] School of Computer Science and Mathematics, Kingston University London, KT1 2EE, UK.

Abstract:

When the underground refuge chamber (URC) operates in the deep sections of mine, it frequently fails to effectively address the issue of indoor environment regulation. The ventilation system can effectively regulate the indoor air quality, serving as a cooling measure as well. An appropriately designed ventilation layout can enhance the uniformity of indoor temperature distribution, thereby improving temperature control performance. In this study, the accuracy of numerical simulation model was validated through experimental method. Numerical simulation was employed to analyze the impact of four factors on the temperature control performance of ventilation system: the distance between inlet and wall (DIW), the type of distance in adjacent inlets (TDIs), the angle of inlet in x-direction and y-direction. The results indicate that: (1) The ventilation layout in case 3 is the most effective. With an initial ambient temperature of 27°C, the effective temperature control duration is extended by 28 h compared to the typical ventilation scheme, reaching 79 h. Additionally, the temperature at 96 h was reduced by 0.4°C, and the waste heat emission efficiency improved by 9.67 %. (2) Given that the alteration of the ventilation layout has a minimal impact on the waste heat absorption efficiency, the variation in the heating rate is predominantly influenced by the waste heat emission efficiency. Consequently, waste heat emission efficiency is utilized to analyze the ranking of the four influencing factors of air inlets layout, which are ordered as follows: x-direction > DIW > TDIs > y-direction.

Keywords: Underground refuge chamber; Air inlets layout; Temperature distribution; Waste heat emission efficiency

Nomenclature			
T	temperature, °C	a_c	the thermal diffusion coefficient, m^2/s
p	pressure, Pa	q_v	the wall heat flow when the air supply volume reaches V_m, W/m^2
Greek symbols		T_τ	the temperature of living room at τ, °C
ω	heating rate, °C/h	T_0	initial indoor air temperature, °C
τ	time, s	T_{con}	temperature of the concrete wall, °C
ρ	density, kg/m^3	T_{air}	indoor air temperature, °C
u	average velocity component, m/s	T_{out}	outlet temperature, °C
k	turbulent kinetic energy, J/kg	T_{in}	inlet temperature, °C
ε	turbulent energy dissipation, J/(kg · s)	S_c	area of the arched section, m^2
α	inverse effective Prandtl number	Aw	the wall area of URC, m^2
h	the convective heat transfer, $W/(m^2 \cdot K)$	Vm	the mass flow of the supply or exhaust outlet, kg/s
λ	the thermal conductivity, W/(m·K)	***Acronyms***	
Subscripts		URC	underground refuge chamber
φ_a	waste heat absorption efficiency	DIW	the distance between inlet and wall
φ_e	waste heat emission efficiency	TDIs	the type of distance in adjacent inlets
x_i	cartesian coordinates in the *i* direction	IAT	indoor air temperature
x_j	cartesian coordinates in the *j* direction	HR	heating rate
x_k	cartesian coordinates in the *k* direction	EM	equivalent mannequin
q_0	the wall heat flow without air supply, W/m^2	MCA	mine compressed air

1. Introduction

Rapid economic growth drives an increased demand for energy [1-2], which, in turn, prompts greater exploitation of deep-seated resources [3]. The coal industry serves as a prime example of a high-risk sector prone to accidents [4]. In the event of an incident, efforts must be made to ensure that those awaiting rescue maintain adequate living conditions until assistance is provided [5-6]. Consequently, refuge stations, havens, or bays were constructed in advance in designated areas of the mine to ensure the safety of miners during emergency situations [7].

URC is an independent enclosed space constructed within the rock mass [8], provides a temporary survival environment for survivors for up to 96 h [9]. As the exploitation of mineral resources deepens [10], and as survivors undergo metabolic changes [11-12], the air quality and thermal environment within the refuge chamber will deteriorate significantly. The air quality during the operation of the refuge chamber directly impacts the safety of the survivors [13]. Furthermore, addressing heat accumulation is a critical issue in managing the URC environment [14].

To regulate the indoor temperature, Du et al. [15] designed a multi-functional ice storage air conditioning system capable of accommodating the living conditions of eight survivors for up to 96 h. Additionally, it is recommended that the implementation of ventilation technology may enhance the temperature control efficiency of the ice storage plate. Zhang et al. [16] developed an ice storage device for high-temperature refuge chamber, utilizing this device to cool the air and deliver it to the chamber, thereby fulfilling the temperature control requirements for 15 refuge personnel when the initial surrounding rock temperature was 32°C. Gao et al. [17] proposed a space-saving phase-change temperature control scheme and determined that the effective control time was 40 h when solely utilizing this phase-change temperature control scheme. The combined application of this scheme with the pre-cooling of the envelope structure can significantly enhance the temperature control capability of latent heat storage [18]. Zhang et al. [19] discovered that the pre-cooling efficiency of surrounding rock was influenced by ventilation volume and ventilation temperature, but was not related to the initial temperature of the surrounding rock. It is evident that within the temperature control scheme of URC, the ventilation system plays a crucial role.

Introducing fresh air into the URC can effectively control indoor air quality [20-22], without incurring additional thermal production [23-24]. Moreover, it contributes to temperature control performance [25]. Additionally, some researchers have established the relationship between ventilation parameters and temperature control performance in their studies with typical ventilation schemes. Jin et al. [26] discovered that room temperature is directly proportional to the initial surrounding rock temperature, heat source intensity, and ventilation temperature, while being inversely proportional to per capita air supply. Zhang et al. [27] found that the heating rate of refuge chamber is inversely proportional to the thermal conductivity coefficient of the rock, its density, specific heat capacity, as well as per capita air supply and wall area, but directly proportional to heat source intensity. Yu et al. [28] emphasized that the supply of fresh air should be determined based on a comprehensive analysis of the number of occupants, building area, and ventilation efficiency. Yao et al. [29] observed that increasing the air supply inlets to reduce airflow speed can enhance comfort levels. It is evident that relying on the typical ventilation system to control temperature in high-temperature URC necessitates a large per capita air supply. This not only increases the difficulty of air supply, but also diminishes the thermal comfort of survivors.

The use of different air flow organizations airflow configurations would generate distinct airflow patterns, thereby influencing thermal comfort and air quality [30-31]. Accordingly, an appropriate ventilation design can create a more uniform indoor thermal environment [32-33], thus providing a conducive atmosphere for survival [34-35]. When the outlet is positioned at the top of the room, the inlet should be located at the bottom rather than at the top. This arrangement enhances air quality in the occupied area and promotes a more uniform temperature distribution at the same horizontal plane [36]. Consequently, employing this ventilation arrangement will enhance comfort. Furthermore, the ventilation configuration utilizing downward air supply and upward air exhaust demonstrates superior ventilation efficacy compared to alternative layouts [37]. After comparing the temperature control efficiency of the single-side air supply scheme with that of the both-sides air supply scheme, Tian et al. [38] found that the both-sides air supply scheme exhibited superior temperature control efficiency. Whereas, when employing the both-side air supply scheme in URC, the indoor temperature distribution will exhibit areas of high temperature accumulation and temperature stratification [19, 26]. Therefore, when implementing the both-sides downward air supply and upward air exhaust scheme in URC, it is essential to modify the layout of the air supply system to reduce the high temperature accumulation area and improve comfort.

In summary, the implementation of typical ventilation systems in URC creates areas of temperature concentration, which adversely affects the efficacy of the temperature control scheme; however, the system effectively maintains indoor air quality. By modifying the airflow organization within URC, the indoor temperature distribution can be made more uniform, thereby enhancing the temperature control performance. Nonetheless, the impact of airflow organization on temperature control in refuge chambers has received little attention. To maintain a low temperature in the indoor living area, this study employs a ventilation scheme that utilizes downward air supply and upward air exhaust. Ultimately, by adjusting the layout parameters of the air inlet to influence indoor air distribution, the indoor temperature distribution is improved.

In this study, the temperature control performance of the both-sided uniform air supply system was evaluated in a 50-person URC, and the accuracy of the simulation model was validated. The objective was to modify the terminal layout and optimize the airflow organization within the URC, thereby enhancing the temperature control performance of the ventilation system. Utilizing a meticulously designed orthogonal simulation scheme, the effects of DIW, TDIs, the angle of the inlets in the x direction, and the angle in the y direction on the temperature control performance of the ventilation system were comprehensively analyzed. This research has extended the effective duration of temperature control and improved the efficiency of waste heat treatment efficiency. Consequently, this study holds significant reference value for the installation of ventilation systems or the enhancement of ventilation layouts in URCs.

2. Methodology

2.1 Evaluation indicators

In order to assess the impact of the air inlets layout on temperature control performance, this study utilizes the following evaluation indicators:

(1) Value of the indoor air temperature (IAT) at 96 h.

(2) Effective temperature control duration.

(3) Temperature distribution.

(4) Heating rate (HR).

(5) Waste heat absorption efficiency.

(6) Waste heat emission efficiency.

The URC is required to provide a temporary living environment for survivors for a duration of 96 h [9]. In the absence of temperature control measures, the IAT of URCs will gradually rise over time. Currently, it is widely accepted that the upper limit of acceptable temperature for survivors within the URC is 35℃ [39]. Consequently, the lower IAT at the 96 h, the longer the effective duration of temperature control, and the more efficient the temperature control performance.

The typical ventilation layout scheme tends to create a high-temperature accumulation zone within the horizontal section of the occupied area, thereby compromising human thermal comfort and the effectiveness of temperature control [27, 34]. In contrast, a lower temperature in the occupied area, coupled with a more uniform distribution, enhances thermal comfort. Additionally, the stratification of hot air at the upper levels facilitates heat dissipation, thereby improving the temperature control performance of the ventilation system. Consequently, the analysis of temperature distribution can provide insights into thermal comfort and thermal emission capacity across various ventilation layouts.

The HR of indoor air varies with time, reflecting the temperature control efficiency of the temperature control scheme at different times. In addition, in order to describe the HR, equation (1) is used to calculate it [40]:

$$\omega_\tau = (T_\tau - T_0)/\tau \tag{1}$$

Where: ω_τ is the heating rate, ℃/h; τ is the ventilation time, h; T_τ is the temperature of indoor air temperature, ℃; T_0 is the initial indoor air temperature, ℃.

When utilizing a ventilation system solely as a temperature control measure, the heat transfer analysis of the living room within the refuge chamber can generally be categorized into five components: human heat dissipation, air heat absorption, wall heat absorption, inlets cooling, and outlets heat emission. Given that human heat dissipation can be considered constant and that the ventilation temperature will remain stable in a deep mine, enhancing the heat absorption capacity of the wall and the heat emission capacity of the outlets will contribute to a reduction in the HR of the IAT, thereby improving the temperature control performance of the URC. Consequently, this paper introduces two indicators: waste heat absorption efficiency and waste heat emission efficiency, to assess the temperature control performance of various ventilation layouts. Equations (2) and (3) are employed for respective calculations [41-42]:

$$\varphi_a = (T_{con} - T_{in})/(T_{air} - T_{in}) \tag{2}$$

$$\varphi_e = (T_{out} - T_{in})/(T_{air} - T_{in}) \tag{3}$$

Where: φ_a indicates the waste heat absorption efficiency; φ_e represents waste heat emission efficiency; T_{con} is the temperature of the concrete wall, °C; T_{air} indicates indoor air temperature, °C; T_{out} indicates outlet temperature, °C; T_{in} indicates the inlet temperature, °C.

2.2 Experimental details

2.2.1 Experimental environment

The experimental site is situated within a teaching building designed to simulate an underground mine in Guizhou Province, China. The horizontal roadway of the building is connected to the inclined roadway, which serves as a ventilation passage. As illustrated in Fig. 1, the chamber features an arched section with an inner circumference of 12.35 m, a vertical wall height of 1.5 m, and an inner vault positioned 3 m above the ground. The total length of the chamber measures 15.85 m, with a width of 5.1 m. The chamber is partitioned into a transition room measuring 1.6 m in length and 4 m in width, and a living room that is 12.6 m long and 4 m wide. The walls of the chamber are constructed from concrete, which has a density of 2300 kg/m³, a specific heat capacity of 920 J/(kg·K), and a thermal conductivity of 1.74 W/(m·K), respectively.

(a)The interior contours (b)The layout of heating tubes

Fig. 1 Diagram illustrating the experimental setup.

As illustrated in Fig. 1, the thickness of the walls on the left and right sides measures 0.55 m, while the thickness of the outer walls at the front and back ends is 0.7 m. The wall at the front of Fig. 1 (a) has a thickness of 0.25 m, serving to separate the transition room from the living room. Each of the three walls at the front and back ends is equipped with a door to facilitate personnel entry and exit. The door is constructed from a 2 mm stainless steel plate, filled with 40 mm thick polyurethane insulation material, and the gaps are sealed with polyurethane foam caulk, effectively reducing the influence of the external environment on the temperature field within the chamber. The living area of the chamber encompasses 50.4 m^2. Given that the per capita building area in the refuge is not less than 1 m^2, the experiment is designed to accommodate 50 refuge personnel by arranging 60 finned copper heating tubes, each with a heat output of 100 W, as depicted in Fig. 1 (b), to replicate the heat production required for 50 survivors during the refuge period [32].

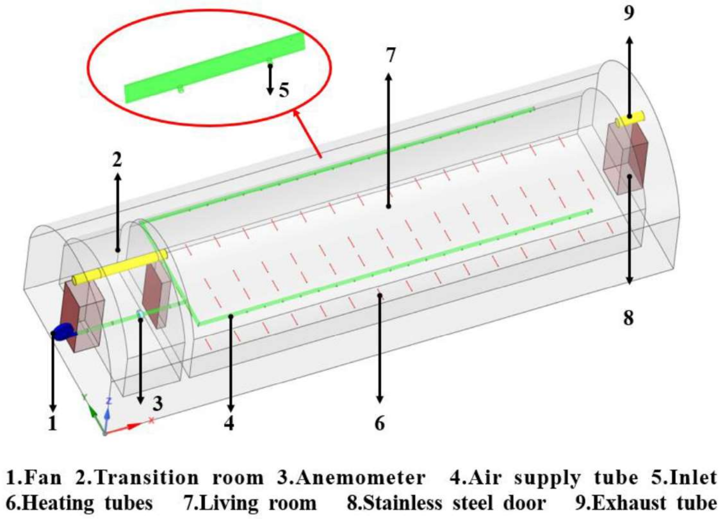

Fig. 2 Schematic diagram of the experiment.

Fig. 2 illustrates the experimental principle, in which the fresh air generated in the ventilation tunnel by the fan is conveyed through a ventilation pipe with a diameter of 0.1 m, positioned at a height of 1.8 m above ground level, to the living room within the refuge chamber. On either side of the ventilation pipes, there are twenty circular vent pipes, each measuring 0.03 m in diameter, that function as air inlets. Ultimately, the fresh air enters the living room through these inlets. Additionally, two emission outlets, each with a diameter of 0.25 m, are located at the front and back of the living room, with their outlets positioned 2.65 m above the ground. The indoor air in the living room will flow through these two emission outlets towards the exterior of the refuge chamber.

2.2.2 Data collection

To monitor variations in air supply temperature, one temperature measurement point was positioned at the anemometer, while 18 temperature measurement points were strategically arranged within the refuge chamber to observe temperature fluctuations, as illustrated in Fig. 3.

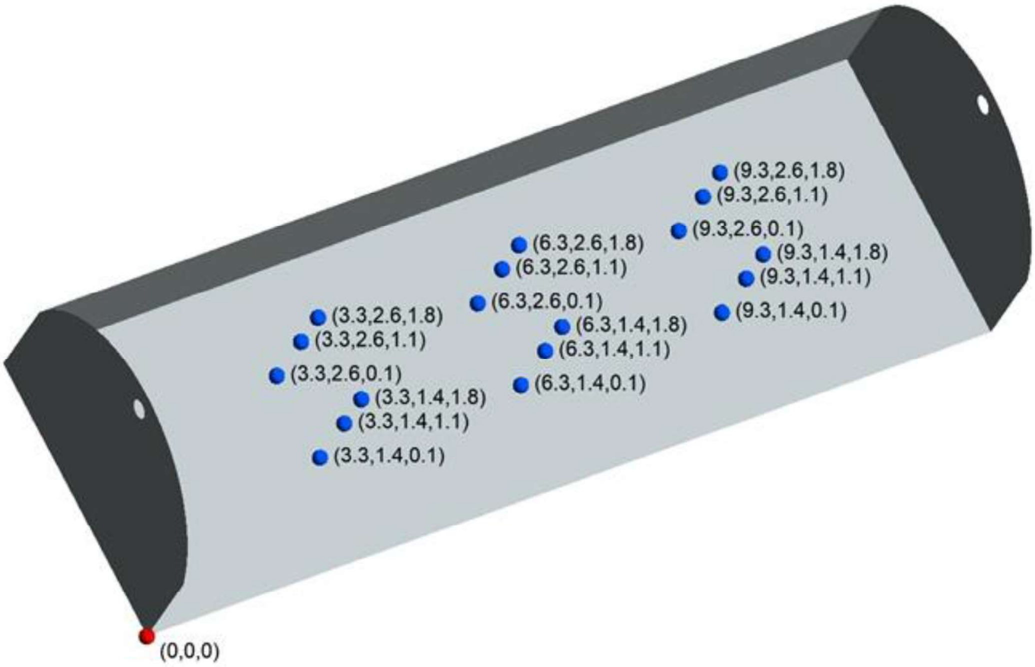

Fig. 3 Coordinate chart of measurement points.

The temperature measurement points within the room are positioned along two vertical sections, each 3.3 m from the ends of the chamber, as well as one central vertical section. The personnel in the URC will remain seated for extended periods within the chamber, with their heads positioned near a horizontal plane at a height of 1.1 m. Additionally, when standing, the heads are considered to be at a height of approximately 1.8 m. Consequently, the measurement points in each section are symmetrically arranged according to three levels: the near-ground level at a height of 0.1 m, the level at 1.1 m, and the level at 1.8 m.

(a) PT100 temperature sensor (b) Temperature acquisition instrument (c) Anemometer

Fig. 4 Data acquisition instrument.

As illustrated in Fig. 4 (a), the temperature measurement device utilizes the PT100 temperature sensor. This sensor is connected to the JK temperature acquisition instrument depicted in Fig. 4 (b), facilitating data storage and retrieval. An anemometer has been selected to measure the wind speed within the ventilation pipe and to calculate the per capita air supply, as demonstrated in Fig. 4 (c).

Through Table 1, the relevant parameters of each data acquisition instrument can be obtained.

Table 1 Parameters of each data acquisition instrument.

Name	Type	Measurement range	Measurement accuracy
Thermocouple	PT100	(-50~200) °C	± 0.01°C
Temperature collector	JK4000	(-200~1800) °C	0.01°C
Anemometer	LSFS-4	(0~9000) m^3/ h	0.02 %

2.2.3 Experimental parameters and processes

Table 2 shows the experimental parameters. Among them, the air supply volume is 900 m^3/h; the heat source intensity is 6000 W; the highest and lowest air supply temperatures are 20.90°C and 14.95°C, respectively; and the height of the air supply inlets is 1.8 m, which is uniformly fixed on the walls on both sides.

Table 2 Experimental parameters.

Name	Parameters
Air supply volume	900 m^3/h
Heat source intensity	6000 W
Air supply temperature	14.95°C~20.90°C
Inlets layout	Height of inlets is 1.8 m, uniformly fixed on the both-sides walls

The primary experimental procedures are conducted as follows:

(1) Activate the data acquisition instrument, monitor the temperature variations, and ensure the proper functioning of the temperature measurement point.

(2) Open the fan and inspect the anemometer to verify that the airflow meets the specified ventilation rate and remains stable.

(3) Upon activating the thermal source controller, the heating pipes will commence operation.

(4) Close the door to prevent external environmental factors from affecting the indoor conditions.

(5) Shut off the heating tubes and open the chamber door to facilitate a reduction in temperature within the chamber.

(6) Compile and analyze the data.

2.3 Numerical details

2.3.1 Geometry simplification

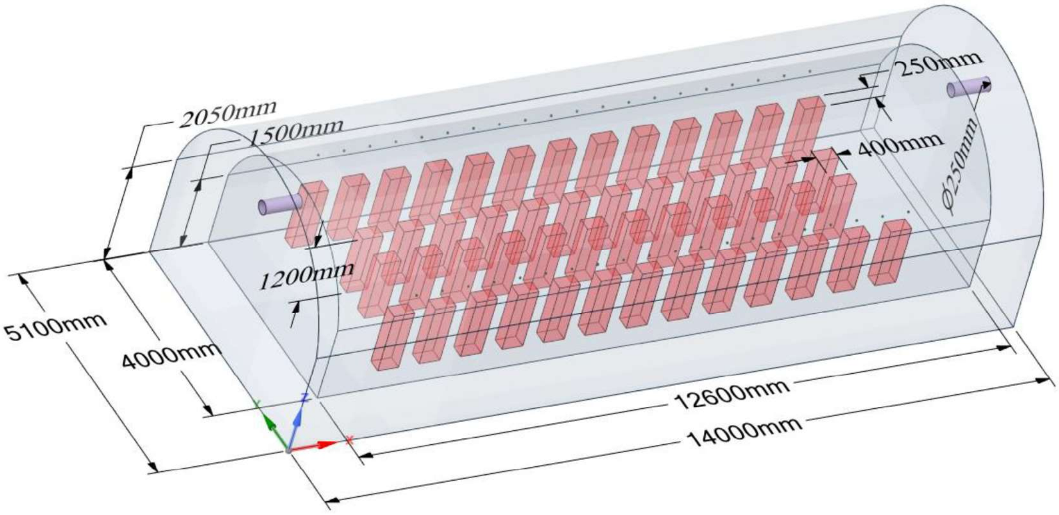

Fig. 5 Geometry of a 50-person refuge chamber.

Given that survivors predominantly remain seated in the living room during the refuge period, this article builds the models of 50-person refuge chamber consisting solely of a living room. The dimensions of the living room in the model are aligned with those observed during the experiment, as illustrated in Fig. 5. Additionally, the wall thickness at both ends is 0.7 m, while the thickness of the remaining walls is 0.55 m. Since the presence of survivors influences the indoor flow field, which cannot be adequately effected by the heating tubes, 50 equivalent mannequins (EM) with dimensions $0.25\times0.40\times1.20m^3$ were utilized as the heat source for simulation calculations [43]. The EMs are arranged in the living room in four rows. The two outer rows of EMs are positioned 0.3 m away from the wall, with a spacing of 0.4 m between the two middle rows of EMs and a spacing of 0.4 m between adjacent EMs within each row. The effect of air in the supply tube is disregarded; thus, 40 air inlets of the same diameter were established in the living room, with a diameter of 0.03 m and a ground distance of 1.8 m from living room.

2.3.2 Influencing factors and orthogonal simulation scheme

Cheng et al. [44] observed that a "cooler feet than head" configuration resulted in improved human comfort. The use of an even both-sides air supply scheme can lower the temperature of low horizontal plane [45]. Consequently, the air inlets are positioned at a height of 1.8 m horizontally, facilitating a more comfortable temperature distribution within the occupied area. Whereas, when employing the both-side air supply scheme in URC, the indoor temperature distribution will exhibit areas of high temperature accumulation in the middle and temperature stratification [19, 26]. Consequently, it is essential to introduce more cold air to the central region to diminish the extent of high temperature accumulation in this area. As is shown in Fig. 6, to achieve this goal, we have identified four strategies: modify the DIW to position the air inlets closer to the central area; adjust the TDIs on both sides to increase the number of air inlets in the central area; alter the angle of the air intake in the x-direction to facilitate greater cold air entry into the central area; and adjust the angle in the y-direction to enhance the airflow for more effective hot air emission.

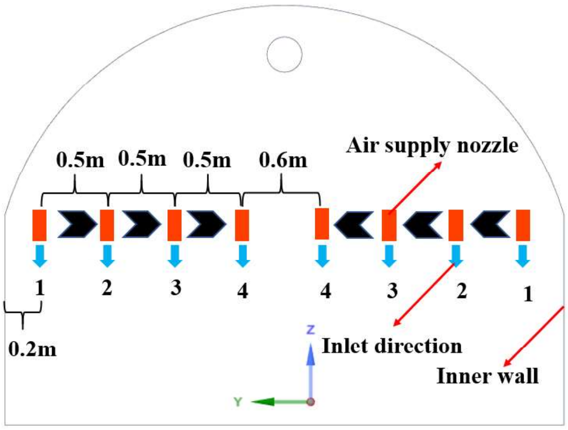

(a) Schematic diagram of the DIW

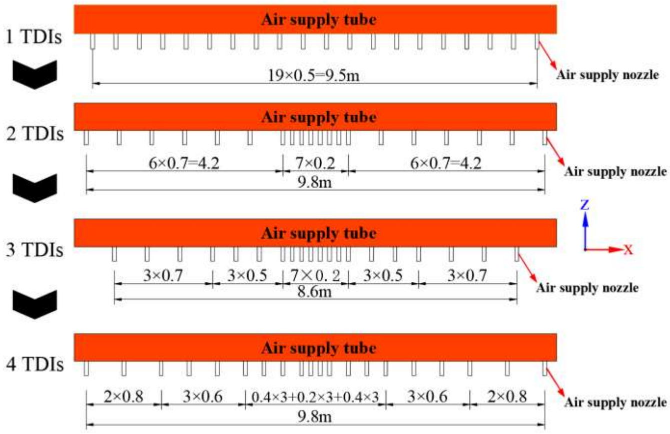

(b) Schematic diagram of TDIs

(c) Schematic diagram of x direction and y direction

Fig. 6 Schematic diagram of influencing factors.

At the same time, four levels are taken for each influencing factor to obtain a smaller range of optimal levels. As illustrated in Fig. 6, the angle of the inlet when oriented perpendicular to the ground is 90°. When the inlet is adjusted in the x and y directions, it varies around the respective x and y axes.

The selection of four factors and four levels necessitates 256 simulations to encompass all working conditions, which is undoubtedly time-consuming and resource-consuming. However, the orthogonal design can significantly reduce the number of working conditions when each factor's levels are evenly considered [46]. The main tool of orthogonal experiment design is orthogonal table.

Additionally, the orthogonal table can be appropriately selected based on the number of factors, the levels of these factors, and the presence of interactions[47]. When four factors, each with four levels, are selected, and the interactions among these factors are taken into account, a minimum of 67 orthogonal simulation cases is required, which remains excessive. Ultimately, as illustrated in Table 3, a 4-factor, 4-level orthogonal table is employed to establish the simulation of cases, thereby minimizing the number of simulations conducted, while disregarding the interactions among the four factors.

Table 3 Initial simulation cases design.

Case	DIW (m)	TDIs	X direction (°)	Y direction (°)
1	0.2	1	90	90
2	0.2	2	60	70
3	0.2	3	30	50
4	0.2	4	0	30
5	0.7	1	60	50
6	0.7	2	90	30
7	0.7	3	0	90
8	0.7	4	30	70
9	1.2	1	30	30
10	1.2	2	0	50
11	1.2	3	90	70
12	1.2	4	60	90
13	1.7	1	0	70
14	1.7	2	30	90
15	1.7	3	60	30
16	1.7	4	90	50

After comparing the results of the above simulation cases, the optimal level and the sub-optimal level of the top three factors were re-orthogonal simulation design. At the same time, their interaction was considered and simulated according to the simulation scheme shown in Table 4.

Table 4 Simulation cases design within interaction.

Case	A	B	A+B	C	A+C	B+C
17	1	1	1	1	1	1
18	1	1	1	2	2	2
19	1	2	2	1	1	2
20	1	2	2	2	2	1
21	2	1	2	1	2	1
22	2	1	2	2	1	2
23	2	2	1	1	2	2
24	2	2	1	2	1	1

2.3.3 Turbulence model

In this study, the air temperature is calculated to range from 20℃ to 40℃, with a dynamic viscosity range of 1.50×10^{-5} m²/s to 1.69×10^{-5} m²/s, indicating that the Reynolds number (Re) in the air emission pipes falls between 38609 and 42833. Consequently, the airflow is characterized as turbulent. For the treatment near the wall, Enhanced Wall Treatment was employed, taking into take into consideration the effects of the pressure gradient and thermal influences, while also considering the full buoyancy effect due to gravity. The governing equations include the continuity equation, momentum equation, and energy equation, as follows [48].

$$\frac{\partial}{\partial x_i}(\rho u_i) = 0 \tag{4}$$

$$\frac{\partial}{\partial x_j}(\rho u_i u_j) = -\frac{\partial p}{\partial x_i} + \frac{\partial}{\partial x_j}\left[u\left(\frac{\partial u_i}{\partial x_j} + \frac{\partial u_j}{\partial x_i}\right)\right] - \frac{2}{3}\mu\frac{\partial u_k}{\partial x_k}\delta_{ij} \tag{5}$$

$$\frac{\partial}{\partial x_j}\left[\rho u_j C_p T - k\frac{\partial T}{\partial x_j}\right] = u_j\frac{\partial p}{\partial x_j} + \left[u\left(\frac{\partial u_i}{\partial x_j} + \frac{\partial u_j}{\partial x_i}\right) - \frac{2}{3}\mu\frac{\partial u_k}{\partial x_k}\delta_{ij}\right] \tag{6}$$

Where: ρ is the density, kg/m³; u is the average velocity component, m/s; x_i, x_j and x_k are the Cartesian coordinates in the i, j *and* k directions, which correspond to the X, Y and Z directions, respectively; p is the average air pressure, Pa; μ is the dynamic viscosity coefficient, N·s/m^2; δ is the Kronecker delta (where $\delta = 1$, when $i = j$ and else $\delta = 0$); C_p is the specific heat, kJ/(kg·K); T is the temperature, ℃.

The geometric model established is based on the actual experimental site, resulting in a large model size. Additionally, during the calculation process, the airflow exhibits complex variations in the vicinity of the EM, whereas in regions further away from the wall and EM, the airflow velocity tends to be lower. Therefore, the RNG k-ε turbulence model has been selected [49]. This turbulence model has good convergence, stability and accuracy in simulating air flow in a ventilated room [50-51]. The transport equations of this model are shown as follows [52]:

$$\frac{\partial}{\partial \tau}(\rho k) + \frac{\partial}{\partial x_i}(\rho k u_i) = \frac{\partial}{\partial x_j}\left(\alpha_k \mu_{eff} \frac{\partial k}{\partial x_j}\right) + G_k + G_b - \rho\varepsilon - Y_M + S_k \tag{7}$$

$$\frac{\partial}{\partial \tau}(\rho \varepsilon) + \frac{\partial}{\partial x_i}(\rho \varepsilon u_i) = \frac{\partial}{\partial x_j}\left(\alpha_k \mu_{eff} \frac{\partial \varepsilon}{\partial x_j}\right) + C_{1\varepsilon}\frac{\varepsilon}{k}(G_k + C_{3\varepsilon}G_b) - C_{2\varepsilon}\rho\frac{\varepsilon^2}{k} - R_\varepsilon + S_\varepsilon \tag{8}$$

Where: G_k is the generation of turbulence kinetic energy due to the mean velocity gradients, G_b is the generation of turbulence kinetic energy due to buoyancy. Y_M is the contribution of the fluctuating dilatation in compressible turbulence to the overall dissipation rate. The quantities α_k and α_ε are the inverse effective Prandtl numbers for k and ε, respectively. S_k and S_ε are user-defined source terms; C_1, C_2, C_3 are constants.

2.3.4 Initialization and boundary conditions

The initialization parameters and boundary conditions applied in the numerical simulation are shown in Table 5. The power output of a single EM is 120 W. During the long-distance air supply process, the air will fully exchange heat with the surrounding rock; therefore, it is assumed that the supply air temperature aligns with the initial ambient temperature. Xiao et al. [53] indicated that when the burial depth ranges from 400 to 600 m, the influence of surface temperature on the temperature of surrounding rock can be disregarded. Consequently, in the deep mine, the initial ambient temperature remains uniform, and the air supply temperature is maintained constantly. Zhang et al. [27] discovered that when the initial ambient temperature exceeds 27°C, merely employing per capita air supply of 0.3 m³/min for the mine compressed air (MCA) scheme is insufficient to satisfy the temperature control requirements within 96 h period. Given that the per capita building area of this model is smaller than that of Zhang et al.'s calculation model, the initial ambient temperature is set to 27°C during calculations to facilitate the identification of the impact of various factors on temperature control performance. Concurrently, the outer wall surface temperature and air supply per capita are established at 27°C and 0.3 m³/min, respectively.

Table 5 Initialization and boundary conditions setting parameters table

Name	Type	Parameter	Remark
Initial air temperature	/	27°C	
Initial wall temperature	/	27°C	Initial conditions
Inlet	Velocity inlet	15 m^3/min; 27°C	
Outlet	Outflow	/	
Outer wall	Fixed temperature	27°C	Boundary conditions
Inner wall	Coupled	/	
EM	Fixed heat flow	120W/person	

2.3.5 Numerical calculation Settings

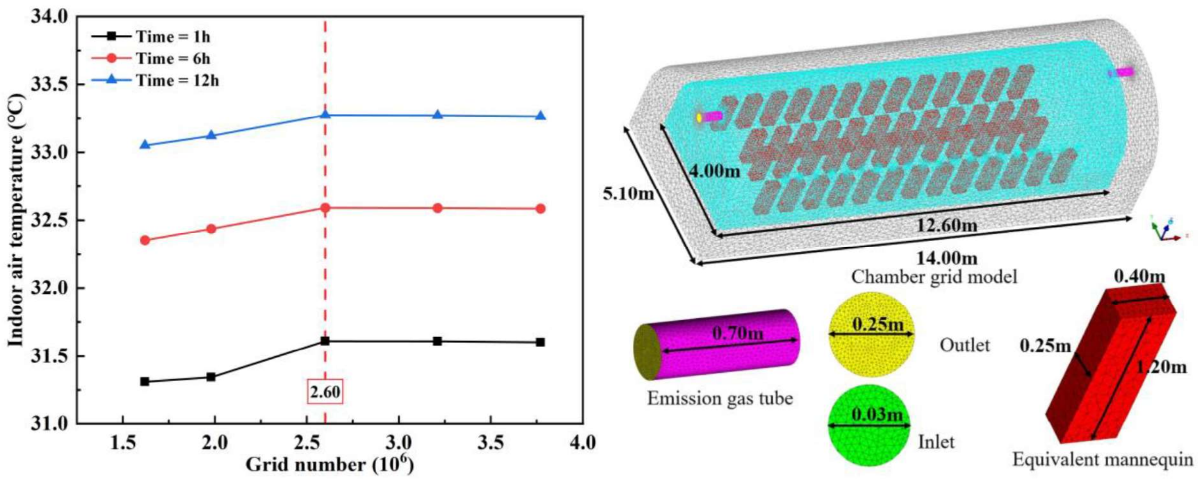

(a) Grid independence validation (b) Numerical model mesh diagram

Fig. 7 Calculate the selection of mesh size.

In ANSYS-ICEM, grid calculation models were generated. To accommodate the complexity of the geometric model, an unstructured mesh was employed. To mitigate the influence of mesh size on the accuracy of the calculation results, five types of meshes were created with mesh counts of 1.62×10^6, 1.98×10^6, 2.60×10^6, 3.12×10^6, and 3.77×10^6. When the initialization and boundary conditions were consistent, numerical calculations were conducted for 12 h across the five mesh models, and the IAT in the chamber over time is illustrated in Fig. 7 (a). It can be observed that when the number of meshes exceeds 2.60×10^6, there are no significant changes in the IAT value at the same moment. Therefore, in the subsequent numerical simulation calculations, it is essential to ensure that the mesh count exceeds 2.60×10^6. Fig. 7 (b) presents the mesh model with a mesh count of 2.60×10^6, which demonstrates a good fit with the geometric model.

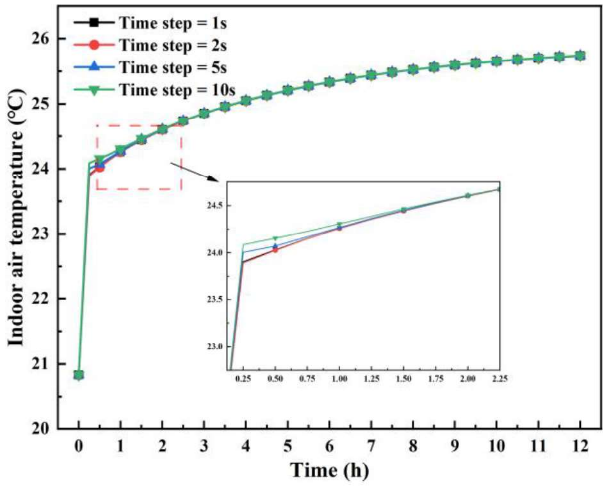

Fig. 8 Time-step validation.

To avoid errors resulting from the improper selection of time steps during calculations, four steps of 1 s, 2 s, 5 s and 10 s were chosen for verification. The variation curve of the IAT in the chamber over time is illustrated in Fig. 8. In the first 2 h, the maximum temperature difference at the same time is 0.18°C, and after 2 h, the calculated results across the four steps of time become consistent. Consequently, different time steps have minimal impact on the calculation results over the 96-hour period. To reduce computation time, the time step of 10 s is selected for subsequent research.

In this study, a pressure-velocity coupling-based simple separation algorithm is utilized. A first-order implicit algorithm is employed, with the pressure term utilizing second-order accuracy, the momentum term employing first-order upwind, and the remaining terms using second-order upwind. The convergence criterion for energy terms is set at 10^{-6}, while the convergence criterion for other terms is established at 10^{-3}[54]. The time step was initially set to 0.1 s and was subsequently adjusted to 10 s after achieving convergence stability.

2.4 Numerical model validation

This study obtained variation data of supply air temperature over time through experiments, which was subsequently compiled into a User Defined Function (UDF) file designated as the inlet temperature for numerical verification simulations. As illustrated in Fig. 9(a), the simulation results were compared with the experimental data. Additionally, to mitigate the potential impact of low air supply temperatures during the experiments on the numerical simulation results, this study conducted a simulation with a higher air supply temperature and compared it with the experimental findings of Zhang et al. [55], as depicted in Fig. 9(b).

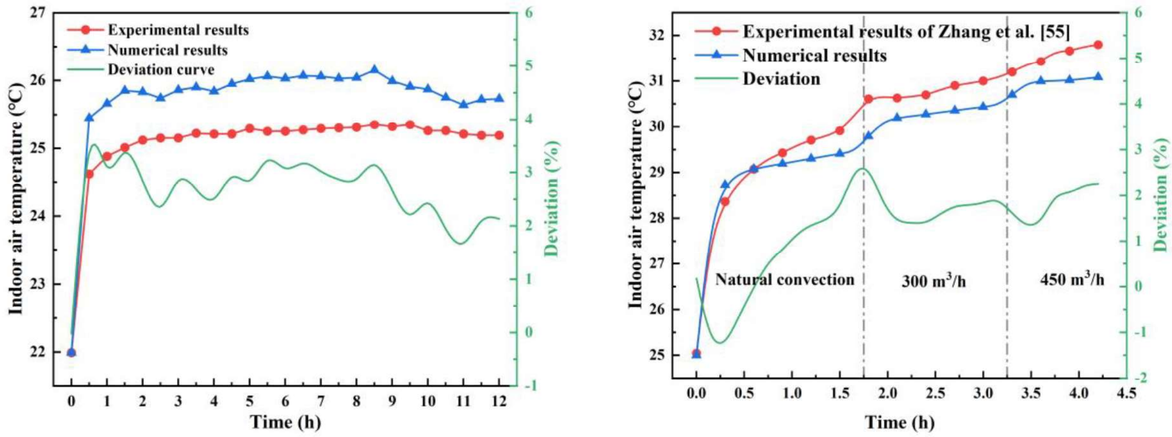

(a) Results of lower supply air temperature (b) Results of higher supply air temperature

Fig. 9 Model validation.

As illustrated in Fig. 9 (a), as the air supply temperature changes in the range of 15-21℃, the temperature variation trends at the measuring points obtained through the two methods are comparable. However, owing to the thermal inertia of the air, changes in the supply air temperature exert a more significant influence on the numerical simulation results. Notably, the maximum temperature difference between the two methods is 0.84℃, with a maximum relative deviation of 3.37 %. As illustrated in Fig. 9 (b), the entire simulation process encompasses two air supply modes and three variations in ventilation volume. During the ventilation volumes of 300 m^3/h and 450 m^3/h, the corresponding air supply temperatures are 34.7℃ and 36.2℃, respectively. As the ventilation volume increases, the maximum temperature differences observed in the three stages of the simulation are 0.81℃, 0.60℃ and 0.72℃, respectively. The corresponding relative errors are 2.67 %, 1.94 % and 2.25%, respectively.

It is evident that the numerical simulation results maintain high accuracy despite variations in both air supply temperature and volume. Consequently, the findings from subsequent studies can be regarded as reliable.

3. Results

3.1 Typical case analysis

3.1.1 Experimental temperature control performance

Fig. 10 illustrates the variation curves of IAT, HR and air supply temperature over a 12 h period for a typical layout featuring uniform air supply on both sides. It is observed that the change in IAT occurs in three distinct stages: the first stage is characterized by rapid heating, occurring within the initial 0.5 h; the second stage represents a slow heating phase, spanning from 0.5 h to 9.5 h; and the third stage is identified as a slow cooling phase, which takes place from 9.5 h to 12 h. Concurrently, the HR after 1 hour will gradually decrease as time progresses.

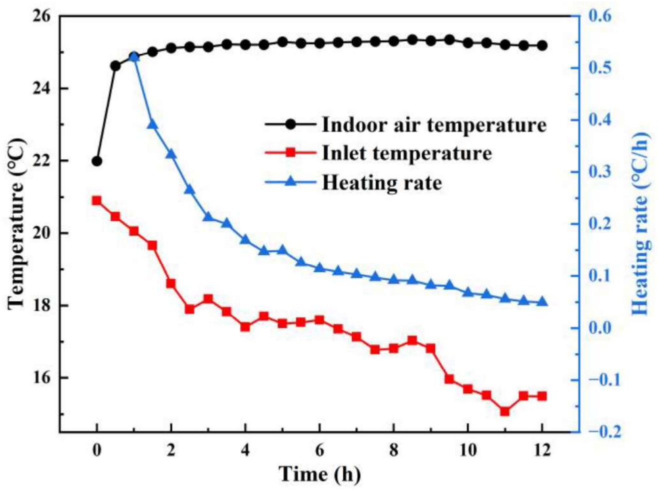

Fig. 10 Variations of temperature and heating rate.

Based on the temperature change curve presented in Fig. 10, it can be observed that the IAT increases from 21.99℃ to 24.62℃ within the first 0.5 h, ultimately reaching 25.19℃ after 12 h. During the rapid heating phase, the temperature difference between the IAT and the wall is minimal, indicating that the IAT is primarily influenced by the heat exchange between the air and the heat source. As the IAT rises, the temperature difference between the air and the wall becomes more pronounced, leading to a gradual increase in heat exchange between the wall and the air. Concurrently, the continuously decreasing air supply temperature progressively enhances the cooling capacity for the URC. The interplay of these two factors results in a gradual decline in the HR during the slow warming phase, culminating in the onset of cooling at 9.5 h.

Fig. 11 illustrates the temperature change curves over time for three vertical cross sections located at the front, middle and back, as well as three horizontal cross sections at heights of 0.1 m, 1.1 m and 1.8 m. This reflects the variations in indoor temperature distribution over time. Overall, the initial 0.5 h represents a rapid heating stage, followed by a slow heating stage thereafter. After 1 hour, the differences in HR across each section at the same time become minimal, resulting in only slight changes in temperature differences among the sections at that moment. Notably, the maximum temperature difference range for the vertical section after 1 hour is between 0.10 and 0.25℃, while the maximum temperature difference range for the horizontal plane after 1 hour is between 0.90 and 1.1℃. It is evident that this ventilation layout scheme will result in significant temperature stratification.

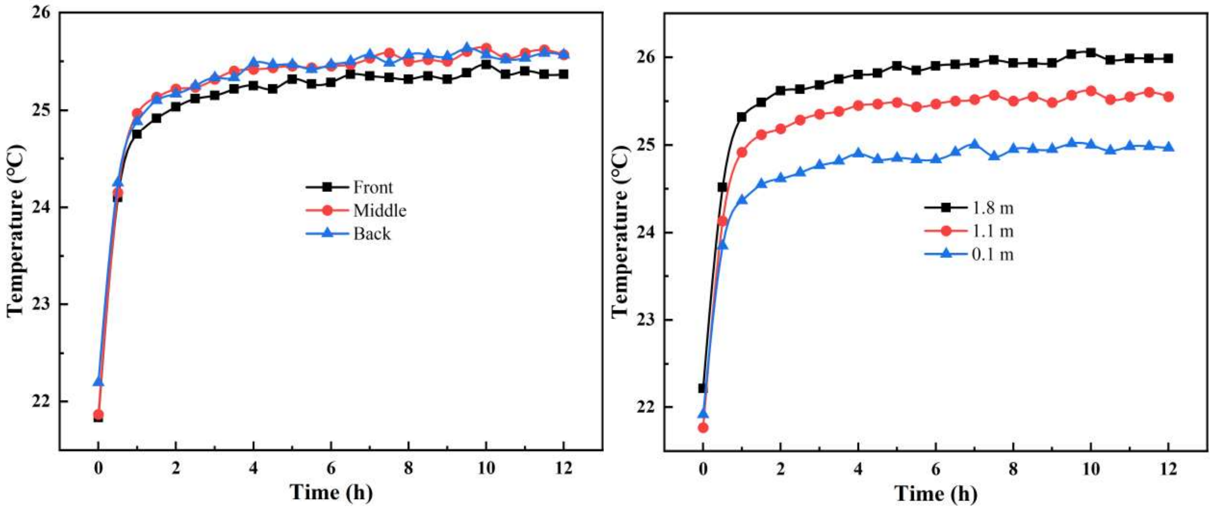

(a) Temperature changes at vertical (b) Temperature changes at horizontal

Fig. 11 Temperature distribution under typical case.

From Fig. 11 (a), it can be observed that the temperature in the front section is the lowest, while the temperature in the middle section is comparable to that in the back section. The heat source is uniformly distributed throughout the space, and the airflow rate at the air inlets is greater at the front end of the chamber and lower at the back end. This results in a higher supply of cold air at the front end and a reduced supply at the back end. Furthermore, the emission outlets are positioned above the two ends of the chamber, leading to a lower efficiency of heat air emission in the middle area compared to the two ends. Due to the disparity in cold air supply and the configuration of the emission outlets, the temperature in the front section is lower, while the temperatures in the middle and back sections are similar.

From Fig. 11 (b), it can be observed that the temperature at the 1.8 m section is the highest, whereas the temperature at the 0.1 m section is the lowest. This temperature stratification is influenced by the airflow. During the flow process, fresh air exchanges heat with the warmer air and heat sources, entering vertically from the walls on both sides. Subsequently, due to the effects of ground barriers and thermal buoyancy, a vortex is formed, with downward movement on both sides and upward movement in the center at the vertical cross-section. Consequently, a temperature stratification phenomenon occurs, where the temperature at a lower level is lower than that at a higher level.

Furthermore, the activity area designated for refuge personnel is primarily located below the 1.1-meter level. Consequently, when designing the ventilation layout, it is essential to ensure that a greater volume of warm air is distributed in the upper region. This approach will help to minimize the consumption of cold energy by hot gases and enhance the emission of hot air. Additionally, positioning the exhaust vents at the upper sections of both walls will facilitate the efficient discharge of hot air from above.

3.1.2 Numerical temperature control performance

When utilizing numerical simulation, the air supply temperature is maintained at a constant level, and the temperature control performance of the typical case involving uniform air supply on both sides is assessed over a duration of 96 h.

According to Fig. 12, the variation in IAT can be categorized into two distinct stages: the rapid heating stage from 0 to 0.5 h, and the slow heating stage from 0.5 to 96 h. The efficiency of waste heat treatment increases progressively over time. However, the heating rate diminishes gradually as time progresses.

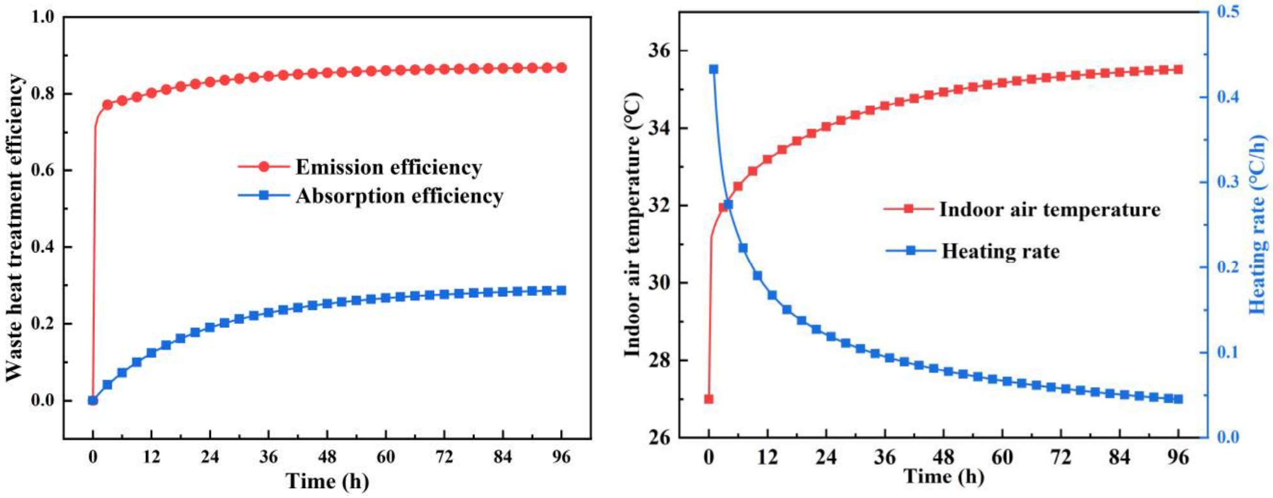

(a) Waste heat treatment efficiency (b) Changes in air temperature and heating rate

Fig. 12 Temperature control performance in 96 h under typical case.

Fig. 12 (a) illustrates the variation curve of waste heat treatment efficiency over time. It is observed that the waste heat emission efficiency is 0.71 at 0.5 h, subsequently increasing gradually until it reaches 0.87 at 96 h. Concurrently, the change rate of waste heat absorption efficiency exceeds that of the waste heat emission rate, starting at a value of 0.01 at 0.5 h and slowly rising over time to reach 0.29 at 96 h. The ventilation layout under typical case results in elevated temperatures in the upper region, leading to a higher HR in that area compared to the whole room. The air at the emission outlets is the hot air from above, which causes the waste heat emission efficiency to progressively increase over time. In the initial stage, the small temperature difference between the IAT and the wall, along with the initial contact between the air and the heat source, results in a greater rate of temperature rise in the room compared to the wall. As time progresses, the temperature difference between the IAT and the wall increases, leading to an enhanced temperature rise rate in the wall, while the corresponding temperature rise rate in the room gradually decreases. This phenomenon results in the observed trend of increasing waste heat absorption efficiency over time.

Fig. 12 (b) illustrates the change curve of the IAT and its heating rate over time. The IAT increased from 27℃ to 31.19℃ within the first 0.5 h, subsequently reaching 35℃ at 51 h, and ultimately attaining 35.51℃ at 96 h. The heating rate of the IAT was measured at 0.385 ℃/h after 1 h, decreased to 0.022 ℃/h at 51 h, and finally reached 0.005 ℃/h at 95 h. It is evident that the HR of the IAT during the slow heating stage gradually diminishes as the efficiency of waste heat treatment improves. Therefore, investigating methods to enhance the efficiency of waste heat treatment will contribute to better temperature control performance in the ventilation system.

Fig. 13 illustrates the contour of temperature distribution at 96 h under typical case. Given that the geometric model is symmetric, the overall temperature distribution is also symmetric. The height of the horizontal plane is designated as a 1.1 m section. It is evident from the Fig. 13 that the area of high temperature accumulation is located in the central region of the horizontal plane, with the highest temperature observed in the middle cross-section. This temperature distribution will result in significant variations in the thermal comfort of refuge personnel situated in different indoor locations. Additionally, the temperature control performance of the ventilation system is inadequate.

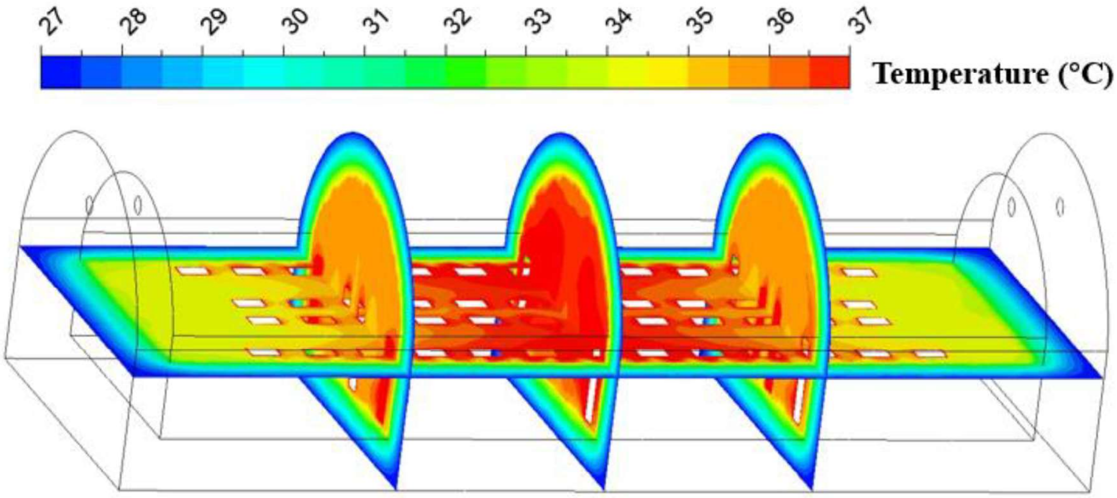

Fig. 13 Temperature distribution at 96h under typical case.

Due to the even distribution of inlets on both sides of the wall, the flow rate in the horizontal plane is minimal in the central region. Consequently, the emission of hot air in this area is sluggish, leading to the formation of a heat accumulation zone over time. Additionally, the positioning of the inlets causes the airflow to generate eddy currents at the vertical section, resulting in elevated temperature accumulation in the central area of each vertical section. Therefore, to achieve improved temperature control performance in the ventilation system, it is essential to investigate the terminal layout of the air supply system to enhance the overall temperature control efficiency.

3.2 Temperature control performance

3.2.1 Uniformity of temperature distribution

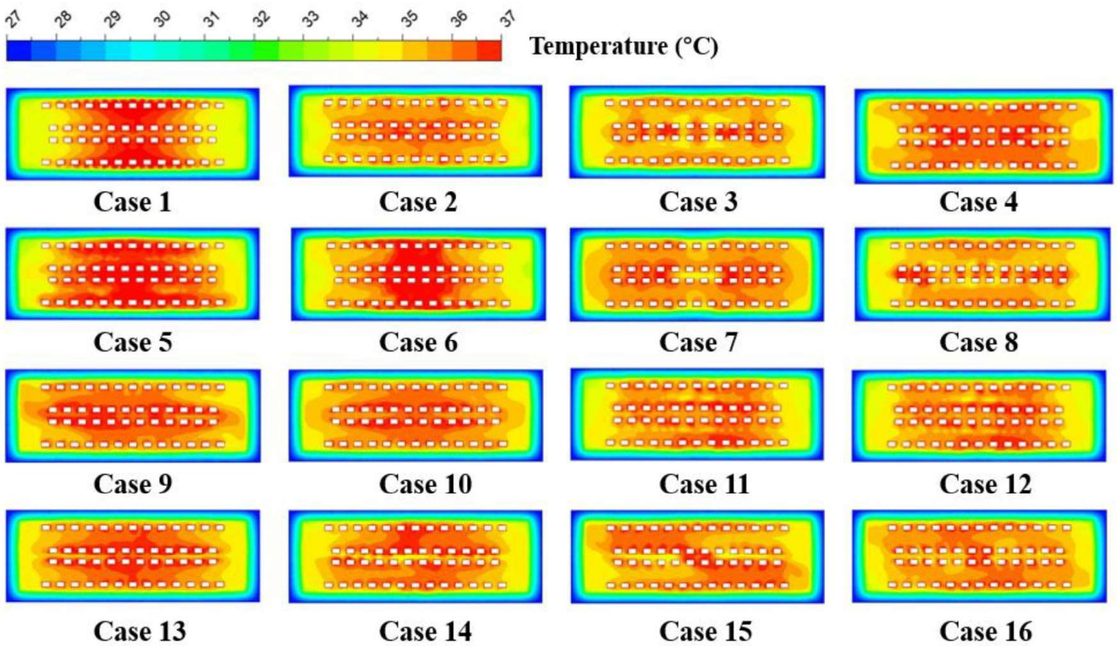

Fig. 14 The contour of temperature distribution under various cases.

Fig. 14 illustrates the contour of temperature distribution at a height of 1.1 meters for each case at 96 h. It is evident that the temperature distribution of the wall is minimally influenced by the ventilation layout, while significant differences are observed in the IAT contour images across the various cases. Additionally, most of the high-temperature areas are located in the central region and around the EM.

In cases 1, 5 and 13, a significant heat accumulation area is observed, whereas the heat accumulation area is relatively small in cases 2, 3 and 8. The temperature distribution in case 2 is the most uniform. In the contour images for cases 3 and 8, a high-temperature accumulation area is present between the middle two rows of the EM, although there are more regions below 35℃ in the central area of the cross-section. The high-temperature areas in cases 9, 10 and 13 are primarily located around the middle two rows of the EM. The distribution of the temperature contour images in cases 15 and 16 exhibits overall central symmetry, while the distribution of the remaining temperature contours is symmetrical as a whole. It is evident that altering the airflow organization can significantly impact the air temperature distribution within the room. Additionally, this adjustment can enhance the temperature control capabilities of the ventilation system and reduce the high-temperature accumulation areas.

3.2.2 Waste heat treatment efficiency and temperature variation within 96h

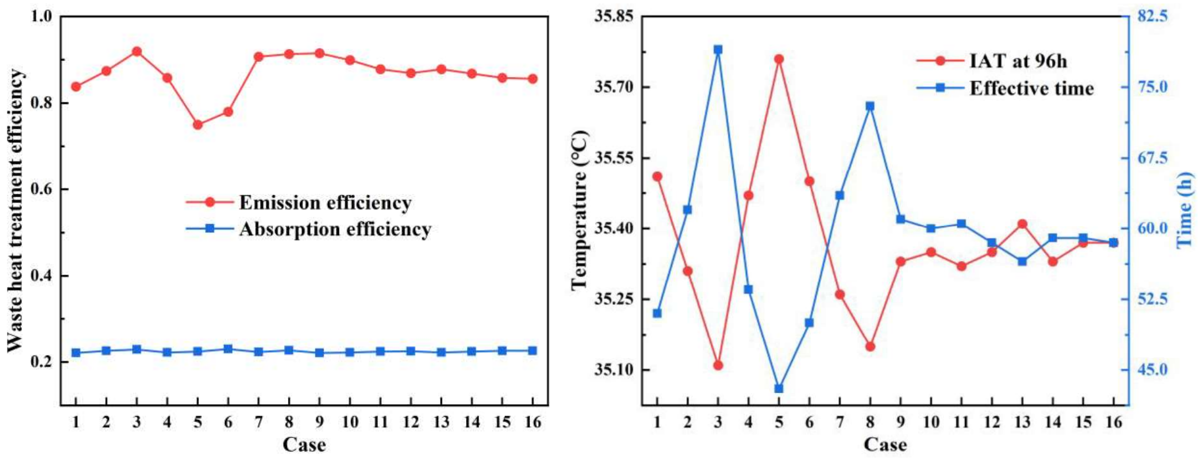

(a) Waste heat treatment efficiency (b) IAT and effective time

Fig. 15 Changes of temperature control performance with ventilation layout.

As illustrated in Fig. 15, to facilitate a more precise comparison of the impact of different ventilation layouts on temperature control performance, an analysis was conducted on the average waste heat treatment efficiency over a period of 96 h, the IAT at 96 h, and the effective duration of temperature control.

Fig. 15 (a) illustrates the average waste heat treatment efficiency across various cases over a period of 96 h. It is evident that the average waste heat emission efficiency varies significantly with changes in the ventilation layout, exhibiting a range of 0.169. In contrast, the differences in average waste heat absorption efficiency among the different cases are minimal, with a range of only 0.009. The average waste heat emission efficiency reaches its peak value of 0.919 in case 3. When compared to the average waste heat emission efficiency of case 1, which stands at 0.838, case 3 demonstrates an increase of 9.67%. Additionally, the waste heat absorption efficiency in case 3 is recorded at 0.229, which is 0.001 lower than the maximum value of 0.230. Conversely, the lowest average waste heat emission efficiency is observed in case 5, at a mere 0.75, while the lowest waste heat absorption efficiency is found in case 9, at 0.221.

Fig. 15 (b) illustrates the effective temperature control duration and the final temperature after 96 h across various cases. It is observed that the maximum effective duration for case 3 is 79 h, while the minimum effective duration for case 5 is merely 43 h. The effective duration for case 1, which employs a traditional ventilation layout, is recorded at 51 h. A comparison of the final temperature control outcomes after 96 h reveals that the room temperature for case 3 is 35.11℃, which is 0.4℃ lower than that of case 1 and 0.65℃ lower than that of case 5.

By analyzing the waste heat treatment efficiency and temperature variations across each case, it is evident that the temperature control performance of case 3 is superior, while that of case 5 is the least effective. Fig. 16 illustrates the variations in IAT and HR over time for cases 1, 3 and 5.

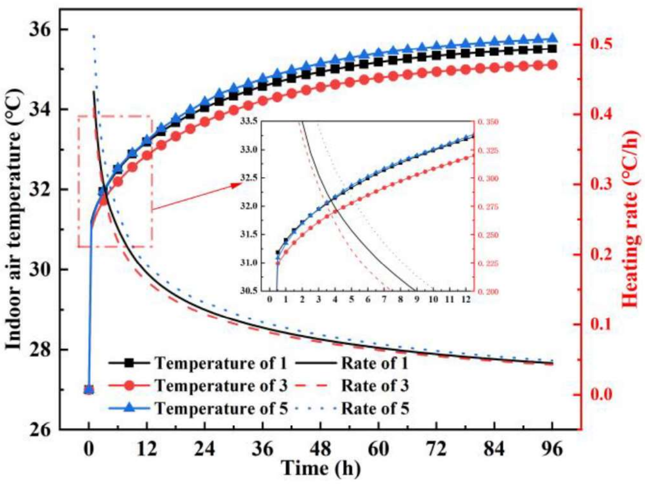

Fig. 16 Curve of IAT and HR with time.

Since the IAT increases rapidly before 0.5 h and then heats up slowly after that point, the starting time of the HR curve is set at 1 h. It can be observed that the IAT of case 3 is the lowest at all times, and the IAT difference between case 1 and case 5 is minimal before 12 h. The IAT of case 5 is slightly lower than that of case 1 before 2 h; however, after 2 h, the IAT of case 5 exceeds that of case 1. Overall, the HR of each case exhibited a decreasing trend over time, with case 5 having the highest HR and case 3 the lowest.

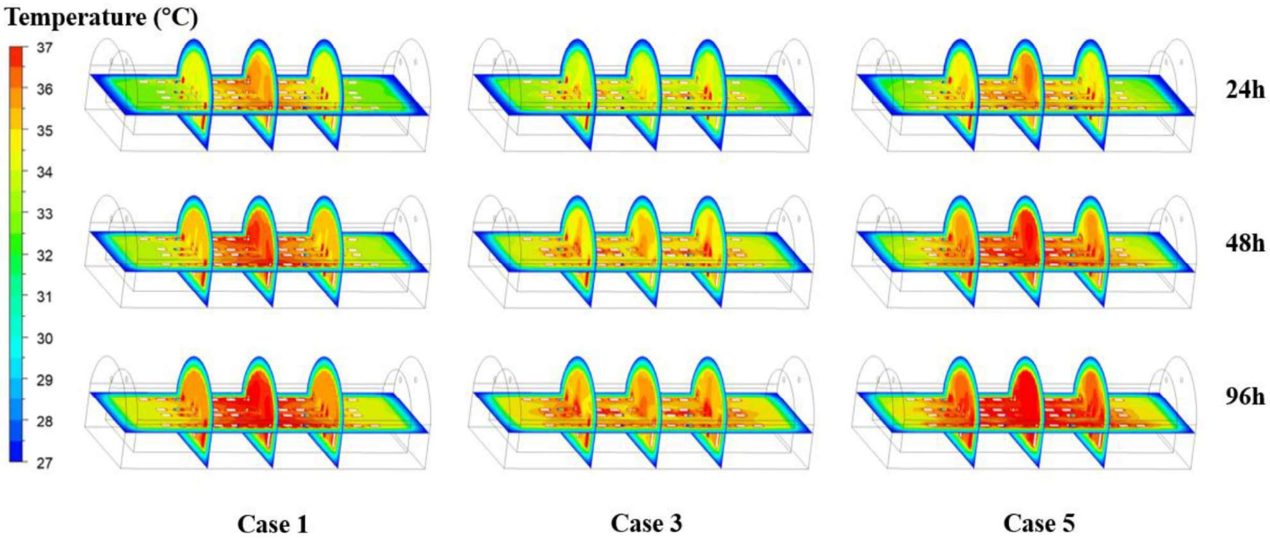

Fig. 17 Temperature distribution of URC at different times.

Fig. 17 illustrates the temperature distribution for cases 1, 3 and 5 over the time intervals of 24 h, 48 h and 96 h. At any given time, the high-temperature area in case 3 is smaller than that of the other two cases. Furthermore, the temperature distribution in this case is more uniform across the horizontal cross-section, while the high-temperature area in the upper section of the vertical cross-section is larger, which facilitates the emission of high-temperature gases. The high-temperature area in the middle cross-section of cases 1 and 5 is significantly greater than that in both end sections, and the high-temperature area in the horizontal cross-section is also concentrated in the middle. This phenomenon indicates that both cases exhibit higher temperatures in the central region and lower temperatures on the sides, which has an inhibitory effect on the emission of high-temperature gases.

This study aims to examine the impact of various factors related to terminal layout on temperature control performance. Subsequently, we will discuss the effects of DIW, TDIs, as well as the angles of the air inlets in both the x and y directions on the temperature control performance of the ventilation system.

3.3 Sensitivity analysis

3.3.1 Effect of the DIW

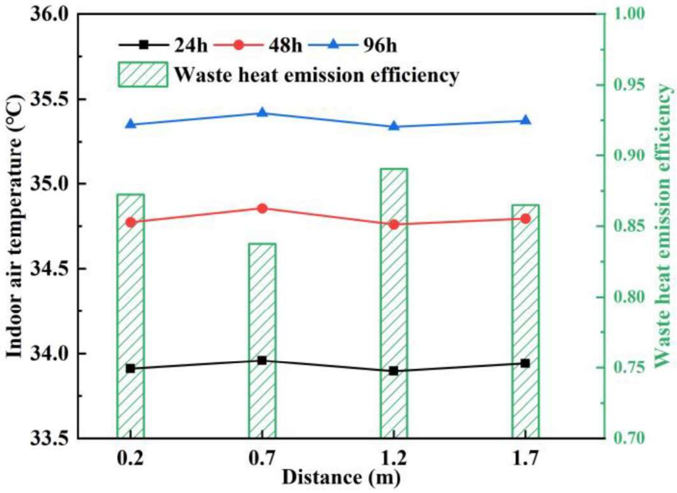

Fig. 18 Influence of the DIW on the temperature control performance.

Fig. 18 illustrates the variations in IAT and waste heat emission efficiency influenced by the DIW. The four levels of this factor are ranked from high to low based on IAT at each moment: 0.7 m, 1.7 m, 0.2 m and 1.2 m. At 24 h, 48 h and 96 h, the temperature differences between the 0.7 m level and the 1.2 m level are 0.06°C, 0.10°C and 0.11°C, respectively. It is evident that as time progresses, the temperature difference between the two levels increases, indicating that the HR at the 0.7 m level is greater than that at the 1.2 m level. Simultaneously, the average waste heat emission efficiency for each level is ranked from high to low as follows: 1.2 m, 0.2 m, 0.7 m and 0.7 m, with their respective values being 0.890, 0.873, 0.865 and 0.838, resulting in a range of 0.052.

The three levels of 0.2 m, 0.7 m, and 1.7 m are situated in proximity to one row of EMs while being distanced from the other EMs on one side. Consequently, after the fresh air interacts with one row of EMs, the cold air within it is significantly depleted. When this air subsequently reaches the other EMs, it is unable to supply sufficient cold air to the surrounding environment. This leads to a non-uniform temperature distribution, thereby diminishing temperature control efficiency. Given that the 0.2 m horizontal supply inlets are located near the walls on both sides, the overall airflow direction across the vertical cross-section exhibits a downward trend on the sides and an upward trend in the center. As a result, a high-temperature zone emerges in the central area at the top of the cross-section, which facilitates the emission of hot air. Furthermore, since the 1.7 m level of the air inlets is closest to the central region, the flow rate in this area exceeds that of the sides, thereby enhancing the emission of heated air. Therefore, the waste heat emission efficiency at the 0.2 m and 1.7 m levels is superior to that at the 0.7 m level. It is evident that the temperature control performance of the ventilation system can be enhanced by modifying the DIW.

3.3.2 Effect of the TDIs

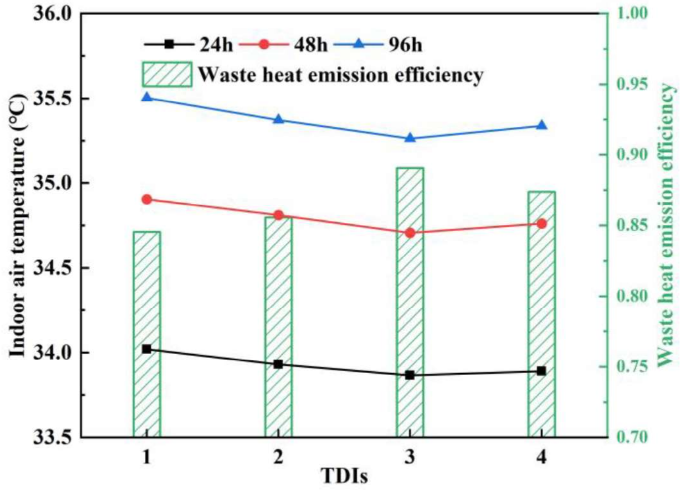

Fig. 19 Influence of TDIs on temperature control performance.

Fig. 19 illustrates the variations in IAT and waste heat emission efficiency influenced by TDIs. The four levels of the factor are ranked from high to low based on the IAT at each moment: 1 TDIs, 2 TDIs, 4 TDIs and 3 TDIs. At 24 h, 48 h and 96 h, the temperature differences between the 1 TDIs level and the 3 TDIs level are 0.15°C, 0.20°C and 0.24°C, respectively. It is evident that as time progresses, the temperature difference between the two levels increases. Concurrently, the average waste heat emission efficiency for each level is ranked from high to low as follows: 3 TDIs, 4 TDIs, 2 TDIs and 1 TDIs, with corresponding values of 0.891, 0.874, 0.856 and 0.845, resulting in a range of 0.046.

If the distance between air inlets is evenly distributed, the IAT in the central area becomes excessively high. Therefore, by increasing the number of supply inlets in the central region, the volume of cold air introduced into this area is enhanced, thereby reducing the temperature. This adjustment also leads to a more uniform temperature distribution within the URC, ultimately improving temperature control performance.

3.3.3 Effect of the air-inlets angles

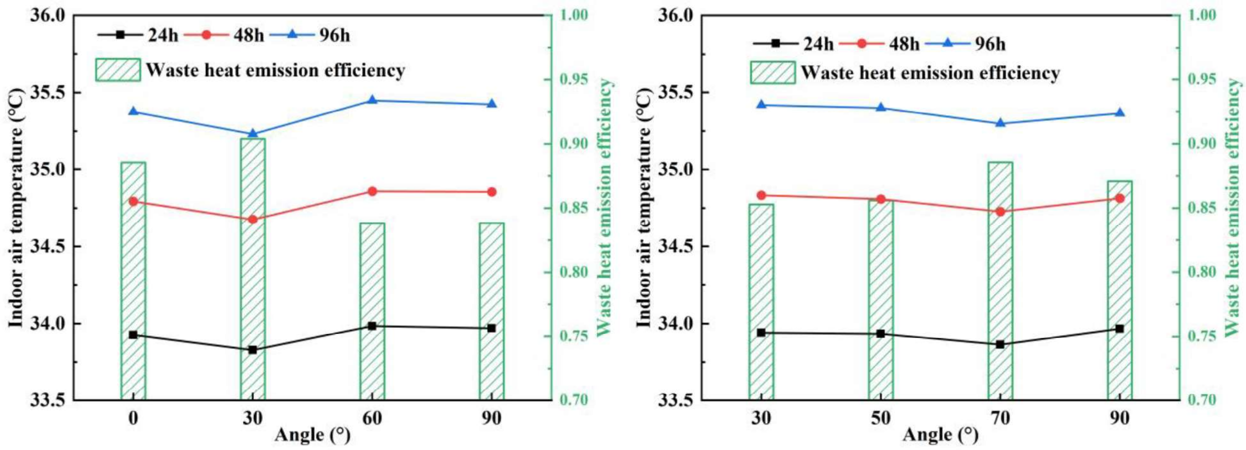

(a) X direction (b) Y direction

Fig. 20 Influence of air-inlets angles on temperature control performance.

Fig. 20 (a) illustrates the variations in IAT and waste heat emission efficiency influenced by the air inlets angle factor in the x direction. It is observed that the IAT at each level, at the same time, is ranked from high to low as follows: 60°, 90°, 0° and 30°. At 24 h, 48 h and 96 h, the temperature differences between the 60° level and the 30° level are 0.16°C, 0.18°C and 0.22°C, respectively. This indicates that as time progresses, the temperature difference between the two levels increases. Concurrently, the average waste heat emission efficiency for each level is ranked from high to low as 30°, 0°, 90° and 60°, with corresponding values of 0.904, 0.886, 0.838 and 0.837, resulting in a range of 0.066.

By altering the air inlets angle in the x direction, the flow velocity of fresh air across the horizontal plane is significantly affected, thereby influencing the temperature distribution. A smaller air inlets angle facilitates the introduction of more cold capacity into the central part of the living area. Conversely, a larger air inlets angle directs more cold capacity towards the sides of the area. Consequently, the temperature control performance at the 0° and 90° levels is suboptimal. When the air inlets angle is set at 30°, the air inlets position, being 0.5 m higher than that of the EMs, allows for a greater influx of cold capacity into the central area. At a 60° air inlets angle, the cold supply is distributed more evenly throughout the survival area, resulting in optimal temperature control performance.

Fig. 20 (b) illustrates the variation of the IAT and waste heat emission efficiency as influenced by the air inlets angle in the y-direction. It is observed that the IAT for each level at 96 h is ranked from highest to lowest as follows: 30°, 50°, 90° and 70°. For 48 h, the ranking is 30°, 90°, 50° and 70°. And for 24 h, the order is 90°, 30°, 50° and 70°. Notably, the lowest temperature recorded at the same time occurs at the 70° level. Furthermore, due to varying heating rates, the highest temperature level shifts from 90° to 30°. At 24 h, 48 h and 96 h, the temperature differences between 30° and 70° are 0.08℃, 0.10℃ and 0.12℃, respectively. This indicates that, with the passage of time, the temperature difference between the two levels continues to increase at a gradual rate. Concurrently, the average waste heat emission efficiency for each level is ranked from highest to lowest as follows: 70°, 90°, 50° and 30°, with corresponding values of 0.886, 0.871, 0.856 and 0.853, resulting in a range of 0.033.

As the air inlets angle in the y-direction decreases, the cold supply to both ends of the survival zone gradually increases, while the cold supply to the center of the survival zone diminishes. This reduction in cooling supply leads to the formation of a high-temperature accumulation area in that region. Additionally, when the air inlets angle changes, the waste heat emission efficiency at both ends of the URC improves. Consequently, the 70° level demonstrates the best temperature control performance, whereas the 30° level exhibits the poorest temperature control performance.

It can be observed that the lowest IAT and the highest waste heat treatment efficiency predominantly occur at the optimal level of the x-direction angle. Consequently, it can be concluded that variations in the x-direction angle exert a more significant influence on temperature control performance, whereas changes in the y-direction angle have a comparatively lesser impact.

4. Discussion

4.1 Optimization of air inlets layout

4.1.1 Significance analysis of impact factors

Table 6 Orthogonal numerical results.

Case	DIW(m)	TDIs	X direction (°)	Y direction (°)	φ_e
1	0.2	1	90	90	0.838
2	0.2	2	60	70	0.874
3	0.2	3	30	50	0.919
4	0.2	4	0	30	0.858
5	0.7	1	60	50	0.750
6	0.7	2	90	30	0.781
7	0.7	3	0	90	0.907
8	0.7	4	30	70	0.913
9	1.2	1	30	30	0.915
10	1.2	2	0	50	0.899
11	1.2	3	90	70	0.878
12	1.2	4	60	90	0.869
13	1.7	1	0	70	0.878
14	1.7	2	30	90	0.869
15	1.7	3	60	30	0.858
16	1.7	4	90	50	0.855
K_1	3.490	3.382	3.352	3.483	
K_2	3.351	3.422	3.352	3.543	
K_3	3.562	3.563	3.616	3.424	
K_4	3.460	3.495	3.542	3.412	
$k_1=(\frac{K_1}{4})$	0.873	0.845	0.838	0.871	
$k_2=(\frac{K_2}{4})$	0.838	0.856	0.838	0.886	
$k_3=(\frac{K_3}{4})$	0.890	0.891	0.904	0.856	
$k_4=(\frac{K_4}{4})$	0.865	0.874	0.886	0.853	
Range	0.053	0.045	0.066	0.033	

To ascertain the influence of DIW, TDIs, and the air inlets angles in both the x and y directions on IAT, a comprehensive analysis of the key influencing factors was conducted by processing the data obtained from orthogonal cases.

As illustrated in Table 6, the average waste heat emission efficiency over a period of 96 h was analyzed. K_i (i = 1,2,3,4) denotes the sum of waste heat emission efficiency for each of the i level of the respective factors, while the Range is defined as the maximum value minus the minimum value of K_i within the same column. A larger range indicates that variations in the level of this factor exert a more significant influence on temperature control performance. The ranges for DIW, TDIs, the x direction, and the y direction are 0.053, 0.045, 0.066, and 0.033, respectively. It is evident that the x direction factor has the most substantial impact on temperature control performance, whereas the y direction factor has the least. Ultimately, the range analysis is conducted based on the orthogonal simulation results, revealing the order of influence of each factor on the temperature control performance of the ventilation system as follows: x direction > DIW > TDIs > y direction.

It can be observed that the optimal horizontal combination does not manifest under the simulation conditions, primarily due to the neglect of the interactions among various factors in the design of the orthogonal simulation conditions. To minimize computational costs, only the optimal levels of the three most significant factors and the second level are taken into account for numerical simulation calculations that consider these interactions, with the y-angle set at 50°. The final results are presented in Table 7. The ranges for DIW, TDIs, DIW+TDIs, X, DIW+X and TDIs+X are 0.013, 0.006, 0.008, 0, 0.031 and 0.001, respectively. It is evident that the DIW+X factor has the most substantial impact on temperature control performance, whereas the x direction factor has the least. Ultimately, the range analysis is conducted based on the orthogonal simulation results, revealing the order of influence of each factor on the temperature control performance of the ventilation system as follows: DIW+X > DIW > DIW+TDIs > TDIs > TDIs+X > x direction. At the same time, the optimal levels combination obtained is: DIW is 0.2 m, 3 TDIs, 1 level of DIW+TDIs, x direction is 30°, 1 level of DIW+X, 2 level of TDIs+X. The ventilation layout of the optimal combination aligns with the optimal case identified in the initial orthogonal simulation scheme.

Table 7 Simulation results within interaction.

Case	DIW (m)	TDIs	DIW+TDIs	X direction (°)	DIW+X	TDIs+X	φ_e
17	0.2	3	1	30	1	1	0.919
18	0.2	3	1	0	2	2	0.890
19	0.2	4	2	30	1	2	0.907
20	0.2	4	2	0	2	1	0.874
21	1.2	3	2	30	2	1	0.867
22	1.2	3	2	0	1	2	0.900
23	1.2	4	1	30	2	2	0.870
24	1.2	4	1	0	1	1	0.900
L_1	1.794625	1.787912	1.789441	1.781622	1.812629	1.780045	
L_2	1.768262	1.774976	1.773446	1.781266	1.750258	1.782842	
l_1	0.897	0.894	0.895	0.891	0.906	0.890	
l_2	0.884	0.887	0.887	0.891	0.875	0.891	
Range	0.013	0.006	0.008	0.000	0.031	0.001	

4.1.2 Temperature control performance in different ambient temperatures

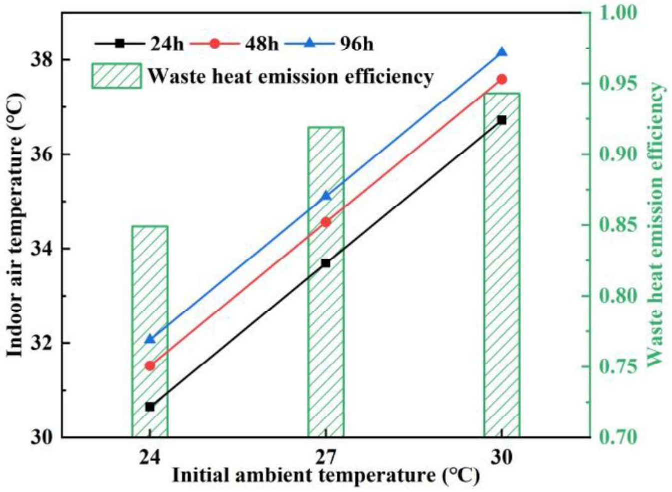

Fig. 21 Temperature control performance changes with ambient temperature.

By varying the initial ambient temperature and conducting a 96-hour numerical simulation under the optimal ventilation layout. The acquired data were compared with the temperature control performance and are ultimately presented in Fig. 21. It can be observed that the temperature difference fluctuation of any two groups at different times is very small, in which the average temperature difference between the working condition with the initial ambient temperature of 27°C and the working condition with the initial ambient temperature of 24°C and 30°C within 96h is 3.04°C and 3.03°C, respectively. Furthermore, as depicted in Fig. 21, when the initial ambient temperature is altered from 24°C to 27°C and 30°C, the average exhaust efficiency of waste heat is recorded at 0.849, 0.919 and 0.943, respectively. These findings indicate that while the HR is minimally affected by changes in the initial ambient temperature, the exhaust efficiency of waste heat tends to increase with rising initial ambient temperatures.

4.2 Heat transfer model analysis

Since the ratio of length to width of the URC in this study is greater than 2, it can be reduced to a cylinder for mathematical analysis. At the same time, the equivalent radius r_i of the inner wall of the cylinder is calculated as $r_i = \sqrt{S_c/\pi}$,where S_c is the area of the arched section [39].

Zhang et al. [56] established the IAT prediction equation under natural convection conditions through mathematical analysis, as shown in equation (9-a):

$$T_a(\tau) = T_0 + q_0\left(\frac{1}{h} + \frac{r_i}{\lambda}\frac{1.13\sqrt{F_0}}{1+0.38\sqrt{F_0}}\right) \tag{9-a}$$

Where: q_0 can be calculated according to equation (9-b):

$$q_0 = \frac{Q}{A_w} = \frac{N \cdot q_e}{A_w} = \text{const} \tag{9-b}$$

Where: F_0 can be calculated according to equation (9-c):

$$F_0 = a_c \tau / r_i^2 \tag{9-c}$$

Where: T_a is IAT, °C; τ is time, s; T_0 is the initial ambient temperature, °C; q_0 is the wall heat flow without air supply, W/m^2; h is the convective heat transfer coefficient between air and wall, W/(m^2·K); λ is the thermal conductivity of wall, W/(m·K); F_0 is Fourier number; N is the number of EMs; q_e is the heating power of an EM, W; Aw is the wall area of URC, m^2;a_c is the thermal diffusion coefficient of the wall, m^2/s.

When a mechanical ventilation system is implemented, the temporal variation of IAT can be represented by equation (10).

$$T_a(\tau) = T_0 + q_v\left(\frac{1}{h} + \frac{r_i}{\lambda}\frac{1.13\sqrt{F_0}}{1+0.38\sqrt{F_0}}\right) \tag{10}$$

Where: q_v is the wall heat flow when the air supply volume reachs Vm, W/m^2; Vm is the mass flow of the supply or exhaust outlet, kg/s.

q_v is calculated as equation (11) :

$$q_v = \frac{N \cdot q_e - C_a \cdot V_m (T_{out} - T_{in})}{A_w} = \frac{N \cdot q_e - C_a \cdot V_m \cdot \varphi_a [T_a(\tau) - T_{in}]}{A_w} \tag{11}$$

Make $n_1 = \left(\frac{1}{h} + \frac{r_i}{\lambda} \frac{1.13\sqrt{F_0}}{1+0.38\sqrt{F_0}}\right)$, $n_2 = \frac{C_a \cdot V_m \cdot \varphi_a}{A_w}$. Subsequently, equations (10) and (11) are organized, leading to the final expression.

$$T_a(\tau) = \frac{T_0 + q_0 n_1 + n_1 n_2 T_{in}}{1 + n_1 n_2} \tag{12}$$

4.3 Comparison of different schemes

To facilitate the calculation of the per capita building area, a per capita heat production rate of 120W is assumed. As illustrated in Table 8, in comparison to the model proposed in this paper, Gao et al. [17] achieved a reduction in effective temperature control time by 39.2 hours, under conditions of a larger per capita building area and a lower initial ambient temperature. Although the encapsulated ice plates (EIPs) temperature control scheme utilized by Xu et al. [33] can maintain effective indoor temperatures for up to 72 hours, it necessitates the construction of ice storage rooms to accommodate substantial quantities of ice. Specifically, for a population of 50 individuals, 420 EIPs must be stored. When the initial ambient temperature is 25°C, the indoor temperature rises by 9.17°C after 96 hours using the MCA temperature control scheme under a typical layout [27]. Given that variations in the initial ambient temperature have minimal impact on the temperature differential between the IAT after 96 hours and the initial temperature, the optimized ventilation layout can reduce this temperature differential by 1°C. Zhang et al. [55] proposed a cooled compressed air temperature control scheme, wherein air is cooled prior to being introduced into the URC. This scheme demonstrates effective temperature control performance in high-temperature surrounding rock. However, ice storage is also required during non-working periods, which diminishes economic viability. By substituting the typical ventilation layout with the optimized ventilation layout, equivalent temperature control can be achieved with a reduced air volume, thereby alleviating the challenges associated with air supply and lowering temperature control costs. When the ventilation system of the cooled compressed air is configured according to the optimized ventilation layout, the same temperature control effect can be attained with less ice storage, provided that the air supply volume remains constant, thus enhancing the economic efficiency of the scheme.

Table 8 Comparison of effects for different temperature control methods.

Method	Heat source intensity (W)	Per capita area (m^2)	IAT (°C)	Ventilation parameter	Temperature control performance
Phase change chair [17]	4656	1.42	25	\	The IAT reaches 35°C at 39.8 h.
Encapsulated ice plates [33]	1032	1.45	28	\	When the heating power increases by 14.3 W, an EIP to be stored.
Compressed air [27]	6000	1.12	25	Both sides evenly layout; 0.3 m^3/min; 25°C	IAT rises to 34.17°C at 96 h. An increase of 9.17°C.
Cooled compressed air [55]	6000	1.60	30	Both sides evenly layout; 0.3 m^3/min; 20°C	IAT rises to 33.70°C at 96 h. An increase of 3.70°C.
Optimized compressed air	6000	1.01	27	Optimized ventilation layout; 0.3 m^3/min; 27°C	IAT rises to 35.11°C at 96 h. An increase of 8.11°C.

4.4 Future work

4.4.1 Application of optimized ventilation system

The ventilation system plays a crucial role in regulating the indoor temperature within the URC through the precooling of surrounding rock, the cooling of MCA, and the phase-change coupled MCA. Following the optimization of the ventilation system, the temperature control performance of the aforementioned temperature control strategies can be enhanced. Concurrently, this optimization can alleviate the challenges associated with air supply and reduce temperature control expenditures. This research has the potential to enhance the temperature control performance in underground gathering areas, which may include environments such as underground shopping malls, subway platforms and train cars.

4.4.2 Future research

This study only conducted an optimization analysis on a single temperature control method, the ventilation temperature control system. However, composite temperature control schemes can complement each other to achieve better temperature control performance and save more temperature control costs. Therefore, it is necessary to research whether this optimized system can improve temperature control performance within composite temperature control schemes. For example, the utilization of phase change materials in the compressed air coupled phase change temperature control scheme depends on the ambient temperature. The research in this paper has obtained the temperature distribution of the occupied area, which can guide the placement of phase change materials in layout.

5. Conclusions

In this paper, an orthogonal method is employed to design a numerical simulation scheme aimed at investigating the impact of the air inlets layout on the temperature control performance of the URC over a period of 96 h. The primary findings are as follows:

(1) Utilizing the optimized ventilation layout of case 3, the IAT can be maintained below 35°C for a duration of 79 h, thereby extending the effective temperature control period by 28 h. At 96 h, the IAT measures 35.11°C, reflecting a reduction of 0.40°C.

(2) The HR during the slow heating phase will diminish as the waste heat absorption efficiency and waste heat emission efficiency increase.

(3) The alteration of the air inlets layout has minimal impact on the efficiency of waste heat absorption. However, it enhances the efficiency of waste heat emission by 9.67 %. Furthermore, the distribution of the IAT can be made more uniform, and the area of high-temperature concentration can be reduced.

(4) The range analysis indicates that the order of influence of each factor on the temperature control performance of the ventilation system is as follows: x direction > DIW > TDIs > y direction.

(5) When the ventilation layout remains unchanged, merely increasing the initial ambient temperature has minimal impact on HR within 96 hours; however, it can enhance the efficiency of waste heat emission.

Originality Statement

The submitted paper is the result of the author's independent research and does not include any other published research findings except for the specifically cited content.

Declaration of competing interest

The authors declare that they have no known competing financial interests or personal relationships that could have appeared to influence the work reported in this paper.

Acknowledgments

The authors would like to thank the financial support from the National Natural Science Foundation of China (NO. 52168013 and NO.51908080), the Natural Science Foundation of Guizhou Province (No. ZK [2022]151 and No. [2020]2004) and the State Key Laboratory of Gas Disaster Detecting, Preventing and Emergency Controlling Open fund Project (No.2021SKLKF10).

References:

[1] S.H. Ali, D. Giurco, N. Arndt, E. Nickless, G. Brown, A. Demetriades, R. Durrheim, M.A. Enriquez, J. Kinnaird, A. Littleboy, L.D. Meinert, R. Oberhansli, J. Salem, R. Schodde, G. Schneider, O. Vidal, N. Yakovleva, Mineral supply for sustainable development requires resource governance, Nature 543(7645) (2017) 367-372.

[2] M.A. Destek, A. Sinha, Renewable, non-renewable energy consumption, economic growth, trade openness and ecological footprint: Evidence from organisation for economic Co-operation and development countries, J Clean Prod 242 (2020).

[3] K. Wang, Q. Li, J. Wang, S. Yang, Thermodynamic characteristics of deep space : hot hazard control case study in 1010-m-deep mine, Case Stud Therm Eng 28 (2021).

[4] M. Gul, M.F. Ak, A.F. Guneri, Pythagorean fuzzy VIKOR-based approach for safety risk assessment in mine industry, J Safety Res 69 (2019) 135-153.

[5] K.A. Margolis, C.Y.K. Westerman, K.M. Kowalski-Trakofler, Underground mine Refuge Chamber Expectations Training: Program development and evaluation, Safety Sci 49(3) (2011) 522-530.

[6] X. Hao, C. Guo, Y. Lin, H. Wang, H. Liu, Analysis of Heat Stress and the Indoor Climate Control Requirements for Movable Refuge Chambers, International Journal of Environmental Research and Public Health 13(5) (2016).

[7] K.E. Karadeniz, S. Nowak, D. Guner, T. Sherizadeh, Evaluation on Underground Refuge Alternatives and Explosion Survivability: a Review, Mining, Metallurgy & Exploration 39(6) (2022) 2311-2331.

[8] Z. Zhang, Y. Yuan, K. Wang, X. Gao, X. Cao, Experimental investigation on Influencing Factors of air curtain systems barrier efficiency for mine refuge chamber, Process Saf Environ 102 (2016) 534-546.

[9] W. Guo, Z. Zhang, H. Wu, L. Ge, X. Liang, R. Mao, Experimental study on cooling and dehumidification performance of an ice storage air conditioner used in underground refuge chamber, Int Commun Heat Mass 146 (2023) 11.

[10] D. Wei, C. Du, Y. Lin, B. Chang, Y. Wang, Thermal environment assessment of deep mine based on analytic

hierarchy process and fuzzy comprehensive evaluation, Case Stud Therm Eng 19 (2020).
[11] Z. Zhang, T. Jin, H. Wu, R. Day, X. Gao, K. Wang, R. Mao, Experimental investigation on environmental control of a 50-person mine refuge chamber, Build Environ 210 (2022).
[12] L. Kajtar, J. Nyers, J. Szabo, Dynamic thermal dimensioning of underground spaces, Energy 87 (2015) 361-368.
[13] Z. Zhang, Y. Yuan, K. Wang, Effects of number and layout of air purification devices in mine refuge chamber, Process Saf Environ 105 (2017) 338-347.
[14] D.S. Yantek, L. Yan, N.W. Damiano, M.A. Reyes, J.R. Srednicki, A test method for evaluating the thermal environment of underground coal mine refuge alternatives, Int J Min Sci Techno 29(3) (2019) 343-355.
[15] Y. Du, W. Gai, L. Jin, W. Sheng, Thermal comfort model analysis and optimization performance evaluation of a multifunctional ice storage air conditioning system in a confined mine refuge chamber, Energy 141 (2017) 964-974.
[16] Z. Zhang, W. Guo, H. Wu, L. Ge, X. Liang, R. Mao, Thermal performance of an ice storage device for cooling compressed mine air in high-temperature mine refuge chambers, Appl Therm Eng 233 (2023).
[17] X.K. Gao, Y.P. Yuan, X.L. Cao, H.W. Wu, X.D. Zhao, D. Yan, Coupled cooling method and application of latent heat thermal energy storage combined with pre-cooling of envelope: Temperature control using phase-change chair, Sustain Cities Soc 42 (2018) 38-51.
[18] X.K. Gao, Y.P. Yuan, X.L. Cao, H.W. Wu, X.D. Zhao, Coupled cooling method and application of latent heat thermal energy storage combined with pre-cooling of envelope: Sensitivity analysis and optimization, Process Saf Environ 107 (2017) 438-453.
[19] Z. Zhang, W. Guo, R. Mao, L. Ge, X. Liang, H. Wu, Performance analysis of an improved temperature control scheme with cold stored in surrounding rock for underground refuge chamber, Appl Therm Eng 236 (2024) 121589.
[20] Z. Zhang, H. Wu, K. Wang, R. Day, Y. Yuan, Air quality control in mine refuge chamber with ventilation through pressure air pipeline, Process Saf Environ 135 (2020) 46-58.
[21] Y. Li, Y. Yuan, C. Li, X. Han, X. Zhang, Human responses to high air temperature, relative humidity and carbon dioxide concentration in underground refuge chamber, Build Environ 131 (2018) 53-62.
[22] J.S.T.W. Shao Hao, Theoretical and numerical simulation of critical gas supply of refuge chamber, International Journal of Mining Science and Technology 26(3) (2016) 389-393.
[23] M.R. Haghnegahdar, M.S. Hatamipour, A. Rahimi, Removal of carbon dioxide in an experimental powder-particle spouted bed reactor, Sep Purif Technol 72(3) (2010) 288-293.
[24] M.R. Haghnegahdar, A. Rahimi, M.S. Hatamipour, A rate equation for Ca(OH) 2 and CO 2 reaction in a spouted bed reactor at low gas concentrations, Chem Eng Res Des 89(6A) (2011) 616-620.
[25] H. Li, Z. Wang, J. Li, L. Wang, X. Kong, M. Fan, Study on thermal comfort of interactive cascade ventilation based on body multi-node thermal demand, Energ Buildings 273 (2022) 14.
[26] T. Jin, Z. Zhang, L. Ge, X. Liang, H. Wu, J. Zhou, R. Mao, Investigation on temperature control performance of an underground confined space under ventilation, Therm Sci Eng Prog 50 (2024).
[27] Z. Zhang, H. Wu, K. Wang, R. Day, Y. Yuan, Thermal performance of a mine refuge chamber with human body heat sources under ventilation, Appl Therm Eng 162 (2019) 114243.
[28] J. Yu, Y. Kang, Z.J. Zhai, Advances in research for underground buildings: Energy, thermal comfort and indoor air quality, Energ Buildings 215 (2020).
[29] T. Yao, Z. Lin, An investigation into the performance of fabric diffusers used in stratum ventilation, Build Environ 81 (2014) 103-111.
[30] X. Tian, B. Li, Y. Ma, D. Liu, Y. Li, Y. Cheng, Experimental study of local thermal comfort and ventilation performance for mixing, displacement and stratum ventilation in an office, Sustain Cities Soc 50 (2019) 12.
[31] T. Yao, Z. Lin, An experimental and numerical study on the effect of air terminal layout on the performance of stratum ventilation, Build Environ 82 (2014) 75-86.

[32] T. Jin, Z. Zhang, L. Ge, X. Liang, H. Wu, R. Mao, Experimental investigation on thermal performance of underground refuge chamber under natural convection and ventilation, Case Stud Therm Eng 52 (2023).

[33] X. Xu, S. You, X. Zheng, H. Zhang, S. Liu, Cooling performance of encapsulated ice plates used for the underground refuge chamber, Appl Therm Eng 112 (2017) 259-272.

[34] Y.J.P. Lin, T.H. Tsai, The push-type displacement ventilation in two series-connected chambers, Build Environ 62 (2013) 89-101.

[35] C. Wang, K. Hu, Y. Liu, A novel ventilation method: Experimental measurement and numerical simulation of vertical single-row inclined slit ventilation, Energ Buildings 324 (2024) 16.

[36] K.B. Fernandez, R. Itokazu, K. Ito, Occupant-centric multicriteria optimization of hybrid personalized HVAC system: Impact of supply inlet layout and return air ratio, Energ Buildings 333 (2025) 20.

[37] R. Zhuang, X. Li, J. Tu, CFD study of the effects of furniture layout on indoor air quality under typical office ventilation schemes, Build Simul-China 7(3) (2014) 263-275.

[38] X. Tian, Y. Cheng, J. Liu, Z. Lin, Evaluation of sidewall air supply with the stratified indoor environment in a consultation room, Sustain Cities Soc 75 (2021).

[39] Y. Yuan, X. Gao, H. Wu, Z. Zhang, X. Cao, L. Sun, N. Yu, Coupled cooling method and application of latent heat thermal energy storage combined with pre-cooling of envelope: Method and model development, Energy 119 (2017) 817-833.

[40] X. Li, H. Yang, R. Mao, H. Wu, X. Liang, J. Zhou, Z. Zhang, Experimental investigation on the temperature control performance of compressed air coupled phase change plate system for underground refuge chamber, Int J Heat Mass Tran 233 (2024).

[41] X. Kong, C. Xi, H. Li, Z. Lin, A comparative experimental study on the performance of mixing ventilation and stratum ventilation for space heating, Build Environ 157 (2019) 34-46.

[42] H. Amai, A. Novoselac, Experimental study on air change effectiveness in mixing ventilation, Build Environ 109 (2016) 101-111.

[43] H. Jin, Z. Zhang, J. Zhou, R. Mao, H. Wu, X. Liang, Study on surrounding rock thermal physical properties on thermal comfort in a ventilated underground refuge chamber, Int J Therm Sci 211 (2025) 109755.

[44] Y. Cheng, Z. Lin, A.M.L. Fong, Effects of temperature and supply airflow rate on thermal comfort in a stratum-ventilated room, Build Environ 92 (2015) 269-277.

[45] S. Zhang, X. Zhang, Z. Lin, Concept and ventilation performance demonstration of graded ventilation, Build Environ 256 (2024) 15.

[46] J. E, D. Han, A. Qiu, H. Zhu, Y. Deng, J. Chen, X. Zhao, W. Zuo, H. Wang, J. Chen, Q. Peng, Orthogonal experimental design of liquid-cooling structure on the cooling effect of a liquid-cooled battery thermal management system, Appl Therm Eng 132 (2018) 508-520.

[47] X. Sun, Z. Shi, J. Zhu, Multiobjective Design Optimization of an IPMSM for EVs Based on Fuzzy Method and Sequential Taguchi Method, Ieee T Ind Electron 68(11) (2021) 10592-10600.

[48] H.A. Hasan, H. Togun, A.M. Abed, N. Biswas, H.I. Mohammed, Thermal performance assessment for an array of cylindrical Lithium-Ion battery cells using an Air-Cooling system, Appl Energ 346 (2023) 15.

[49] V. Yakhot, S.A. Orszag, Renormalization group analysis of turbulence. I. Basic theory, J Sci Comput 1(1) (1986) 3-51.

[50] Z. Lin, L. Tian, T. Yao, Q. Wang, T.T. Chow, Experimental and numerical study of room airflow under stratum ventilation, Build Environ 46(1) (2011) 235-244.

[51] J. Li, A. Li, X. Ren, X. Zhang, J. Guo, J. Che, Comparative studies on the ventilation performance and obstacle deflection effect of attached ventilation in underground generator halls, Build Environ 274 (2025) 112730.

[52] W. Guo, Z. Zhang, X. Liang, H. Wu, L. Ge, R. Mao, Numerical study on the heat transfer performance of mine ice-

storage cooling device, Int J Heat Mass Tran 223 (2024) 125255.

[53] Y. Xiao, X. Liu, R. Zhang, Calculation of transient heat transfer through the envelope of an underground cavern using Z-transfer coefficient method, Energ Buildings 48 (2012) 190-198.

[54] X. Zhao, Y. Wu, H. Yang, C. Wang, N. Gao, J. Zang, Prediction of airflow rate and analysis of driving forces for natural ventilation in underground corridors, Energ Buildings 313 (2024).

[55] Z. Zhang, W. Guo, X. Gao, H. Wu, R. Mao, Investigation on temperature control based on cooled mine compressed air for mine refuge chamber with high-temperature surrounding rock, Int J Therm Sci 187 (2023).

[56] Z. Zhang, R. Day, K. Wang, H. Wu, Y. Yuan, Thermal performance analysis of an underground closed chamber with human body heat sources under natural convection, Appl Therm Eng 145 (2018) 453-463.